Chapter 2: Radial Differential Mobility Analyzer for One Nanometer Particle Classification[*]

2.1. Introduction

Nanometer-sized aerosol particles are encountered extensively in research ranging from atmospheric science to nanotechnology. These particles form in the atmosphere through homogeneous nucleation of products of photochemical reactions. Originating as small clusters, these molecular-sized particles grow by condensation and coagulation. Nanoparticle synthesis in aerosol reactors proceeds similarly via homogenous nucleation and subsequent growth. For these and numerous other applications, measurements of the particle size distribution provide important insights into the growth dynamics of the aerosol. Furthermore, the ability to measure the size of nanomaterials is critical for applications in nanotechnology because optical, electrical, and magnetic properties at the nanoscale are size dependent.

The preferred instrument for measuring submicron aerosol particle size has been the differential mobility analyzer (DMA).[*1-3*] This instrument classifies charged particles according to their electrophoretic migration velocity in an electric field applied across a laminar, particle-free sheath flow, usually in the channel between coaxial cylindrical electrodes (cylindrical DMA). Charged particles are transmitted when their

---

[*] "Aerosol Science & Technology: Radial Differential Mobility Analyzer for One Nanometer Particle Classification," (42):53-59. 2009. Mount Laurel, NJ. Reprinted with permission."

migration velocity is near a value determined by instrument design as well as sheath flow rate, Q_{sh}. The ratio of the migration velocity, $v_{m,}$ to the applied electric field, E, is called the particle mobility, Z_P, which is an inverse function of particle mobility diameter, D_p. This dependency implies that the smaller a charged particle is, the larger is its mobility and, thus, a smaller electric field will be required to reach the transmitted migration velocity of a given instrument ($v_m = Z_pE$). Particles with a particular Z_p will be maximally transmitted by properly setting E or, equivalently, the voltage V applied across the instrument electrodes.

Inherently, DMAs can resolve small differences in particle mobility. When diffusion is not important, the best attainable mobility resolution depends on the ratio of the volumetric flow rate of the sheath gas to that of the aerosol, Q_{sh}/Q_a.[*4-5*] This resolution is degraded by Brownian diffusion, which becomes important when the electrostatic potential energy of the migrating particle is small compared to its thermal energy. In this diffusion-limited regime, the theoretical resolution scales with $V^{1/2}$, which limits resolution for small particles.

To achieve high resolution classification of small particles requires making the residence time in the classification region small or correspondingly making the transmitted v_m large. When this condition is met, a high mobility particle (small particle size) can be classified at a high applied voltage. A short classification region is a straightforward way to reduce particle residence time.[*6-7*] Further improvements can be achieved by combining a short column with a large sheath flow rate.[*8-10*]

In contrast to the cylindrical DMA, Zhang et al.[*11*] and Fissan et al.[*12*] demonstrated a radial DMA (RDMA) design, where the sheath gas flows radially inward between two flat electrodes (disks). The aerosol was introduced near the edge of the "primary" electrode and the charged particles were allowed to migrate toward the "counter" electrode in a uniform electric field. The combined flow was subsequently split unevenly between two outflow ports in the center of the electrodes. A small flow (classified flow, Q_s) was directed through the counterelectrode (across from the aerosol inlet annular slot) for further transmission to a particle detector; the remaining flow (excess flow, Q_e) exited through the center of the primary electrode. The initial RDMA was capable of classifying particles larger than 5 nm in diameter. In order to detect smaller particles, the migration velocity of those particles that are transmitted through the classifier must be increased. However, unlike in the cylindrical DMA design, the particle migration velocity of the original radial DMA design cannot be arbitrarily increased by increasing the sheath gas flow rate. A larger sheath flow leads to a correspondingly larger excess flow, which may cause turbulence in the excess outlet port. Turbulence generally degrades the resolution of the instrument and must be avoided. Alternatively, a reduction in particle residence time can be accomplished by using a smaller sizing region, and this approach was chosen for the new RDMA design.

In this section, the details are reported on the design, construction, and calibration of a RDMA, capable of classifying particles with sizes between 1 and 13 nm. As compared to the earlier RDMA design, the modified version reduces the residence time, first, by decreasing the distance between the aerosol inlet and sampling outlet, and second, by modestly increasing the sheath flow rate, while still avoiding turbulence. Instrument calibration is performed by employing gas ions as monodisperse particles in the 1 to 2 nm size range.

2.2. Experimental Method

2.2.1. Instrument Design

The goal of this work was to design an RDMA capable of nanoparticle classification down to one nanometer for use as an *in situ* diagnostic in nanoparticle synthesis reactors.[*13*] De la Mora and co-workers[*7, 9-10*] have demonstrated high resolution sizing in the one nanometer range by operating a short-column cylindrical DMA at very high flow rates (i.e., 500–2200 L min^{-1}). Such operation is impractical when instrument portability or power consumption is important or when the sheath gas must be of high purity to avoid trace impurity contamination. In such applications, the instrument must operate at a low sheath flow rate (~10 L min^{-1}).

In an RDMA, the mobility of particles transmitted with the highest efficiency is given by[*11*]

$$Z^* = \frac{Q_{sh}+Q_e}{2\pi(R_i^2-R_o^2)}\frac{b}{V} = \frac{Q_{sh}+Q_e}{2\pi(R_i^2-R_o^2)}\frac{1}{E}, \tag{2.1}$$

where R_i is the radius of the aerosol inlet to the classifying region, R_o is the radius of the sampled flow outlet port, b is the spacing between the electrodes, and V is the applied voltage. As in the original RDMA, R_o is set equal to 2.4 mm to match the inner diameter of 1/4" tubing, and an electrode spacing $b = 10$ mm is selected so that the device can operate up to $V = 10$ kV, while avoiding electrostatic breakdown when classifying the largest (lowest mobility) particles.

We are concerned with classification of particles in the free molecular limit, for which the electrical mobility of a singly charged particle is

$$Z_p = 0.441 \frac{q(kT/m)^{0.5}}{pD_p^2}, \tag{2.2}$$

where q is the elementary unit charge ($1.602 * 10^{-19}$ coulombs), k is the Boltzmann constant, T is the temperature, m is the mass of the gas molecules, p is the gas pressure, and D_p is the particle mobility diameter. Equation (2.2) is a free-molecular expression that describes well the correlation between diameter and particle mobility for the size range of interest in this study, but deviates from the transition regime expression for particle mobility by 4.6% for a mobility diameter of 10 nm. By combining equations. (2.1) and (2.2), we find that RDMA classification of 1 nm particles requires an entrance radius of $R_i \approx 7.5$ mm when the sheath flow rate is $Q_{sh} = 10$ L min^{-1} and the operating voltage is $V = 60$ V. Due to the reduced volume of the classifying region, the nano-RDMA should be more sensitive to electric field nonuniformities than the earlier design and require experimental characterization of the instrument.

While similar to the original RDMA,[*11*] the new design (termed "nano-RDMA" in the discussion that follows) incorporates several key changes. The first and most significant difference is the radius (labeled R_i in figure 2.1) of the circular slit where the aerosol is introduced that has been reduced from 50 to 7.5 mm. Second, the RDMA[*11*] achieved a resolution in the high voltage limit that was lower than that predicted for non-diffusive particles. It was later found (unpublished) that this was due to a combination of (1) imperfect concentricity between the knife edge and the inner surface that forms the annular aerosol entrance slot, and (2) a less-than-ideal pressure drop through that slot. In the present design, mounting of the knife-edge ring has been modified to ensure concentricity, while permitting adjustment of the aerosol inlet gap height with high precision. The knife edge (labeled in figure 2.2) and inner electrode are machined from

304 stainless steel (SS) to have a slip-fit tolerance on the radius, thereby ensuring concentricity and eliminating any gap through which the aerosol can leak. Precision shims were used to set and optimize the aerosol inlet gap. A shim thickness of 0.44 mm was found to give a minimum in the line width of the ion mobility distribution. Smaller gaps resulted in loss of signal that was attributed to diffusion losses in the inlet gap.

As in the original RDMA design, the aerosol is introduced tangentially into a continuous annular channel (so-called racetrack) between the pieces defining the inlet. A high voltage bias is applied to the aerosol entrance electrode; electrical contact is made through a screw (not shown), which is inserted through the top plate. Opposite this biased electrode is the counterelectrode that is grounded through a Swagelok union. The classified aerosol exits through a port in the center of the counter electrode.

The remaining pieces were made of white Delrin (except as noted). These include the outer shell, the top plate, the sheath gas inlet, the conical excess outlet, the inlet extension (not pictured) and a sheath gas distributor (made of porous polyethylene sheet with an average pore diameter of 25 μm). These pieces are scaled versions of parts from the original design with two exceptions:

(1) The conical excess outlet was designed to fit inside the inner electrode from the top rather than being press fit from the bottom, as in the original RDMA. This piece is made of Delrin (dielectric). Computational fluid dynamics simulations performed using COMSOL Multiphysics indicated that the dielectric surface distorts the uniformity of the electric field within the classifying region. Field distortion was avoided by affixing a thin, metallic wire mesh to the bottom of the conical port, in electrical contact with the inner electrode. Operation of the RDMA with the conductive mesh yielded

higher particle transmission efficiency than observed in preliminary experiments without the mesh, thus confirming the simulation prediction. All data presented herein were obtained with the mesh in place.

(2) In the first design of the nano-RDMA, the aerosol was introduced directly into the racetrack through a grounded Swagelok fitting attached to the outer shell. The strong electric field, produced between this fitting and the biased upper electrode, caused particle loss to walls before entering the classification region.[*14*] To avoid this problem, the Swagelok fitting was moved away from the top electrode by incorporating a 20 mm long Delrin tube. The additional inlet length is expected to result in particle loss to the walls by diffusion. Two alternative approaches were also considered. First, the inlet tubing could be biased to the same potential as the upper electrode. For safety reasons, this option was not implemented. The second alternative was to maintain the upper electrode at ground potential and to bias the bottom electrode. This approach runs into the same issue it was attempting to fix and is less desirable since particle loss would occur in a section where the particles have already been classified.

2.2.2. Instrument Calibration

The performance of the new RDMA design was evaluated by using molecular ions (tetra-alkyl ammonium halides) based on the work and reported mobilities of Ude and de la Mora.[*15*] The molecular ions were produced by electrospraying solutions of the analyte species. The liquid delivery apparatus consisted of an Erlenmeyer flask (125 mL) fitted with a stopper through which two pieces of plastic tubing were inserted as depicted in figure 2.3. One tube was connected to a regulated air supply with fine pressure control (±0.1 psi). The other tube was immersed into the liquid and was connected to a stainless-steel capillary tube (O. D. ≈ 1.6 mm and I. D. 127 μm) that served as the electrospray nozzle. The nozzle was biased to 3.5 kV with respect to a fitting (cross) into which the capillary tube was inserted, through a threaded Delrin rod for electric isolation. Equal nitrogen flows (0.6 L min^{-1} total flow) introduced through the side arms of the cross carry the electrosprayed ions through the outlet port. The electrospray nozzle and aerosol outlet were positioned vertically to prevent dripping that might cause an electrical short.

The calibration standards were ions of tetra-alkyl ammonium salts (tetra-propyl ammonium iodide (TPropylAI), tetra-butyl ammonium iodide (TButylAI) and tetra-heptyl ammonium bromide (THeptylAB)). Solutions were prepared that contained 0.47, 0.27 and 0.20 mmol L^{-1} of these analytes, respectively, in 1-propanol (Sigma Aldrich, St. Louis, MO, 99.7% purity); the analyte concentrations are one-hundredth of those used in the work of Ude and de la Mora.[*15*] The substantial dilution ensured that mostly monomeric tetra-alkyl ammonium ions (R_4N^+, M^+) and “dimers” ($(R_4NX)R_4N^+$, M_2X^+) were produced, thereby allowing unambiguous peak assignment without the need for coupling the RDMA to a mass spectrometer. Additional solutions with tetra-ethyl ammonium iodide (TEthylAI), tetra-pentyl ammonium bromide (TPentylAB) and tetra-hexyl ammonium bromide (THexylAB) in 1-propanol at concentrations of 0.20 mmol/L were employed to produce ions with similar mobilities. For TEthylAI (as well as tetra-methyl ammonium iodide), the crystals did not dissolve completely in 1-propanol and the actual dissolved concentration was unknown. The mobilities of the latter three salts have not been previously measured by DMA.

A sheath flow rate of 10 L min^{-1} was chosen for the calibration experiments. The combined sheath flow and aerosol inlet flow are split so that the excess flow rate is 10 L min^{-1} and the sampled flow rate is 0.6 L min^{-1} (i.e., $Q_{sh} = Q_e$ and $Q_a = Q_s$). While the choice of aerosol flow rate was fixed to mimic the operating conditions of a nanoparticle synthesis reactor, the sheath flow rate of 10 L min^{-1} was found to produce the narrowest distributions of the molecular ions. The device should be capable of operating at higher aerosol flow rates, but additional optimization of the aerosol inlet gap might be necessary.

Molecular ion concentration was calculated from the current output of a home-made faraday cup electrometer as a function of voltage applied to RDMA electrodes. A computer with a 16-bit analog output channel was used to remotely program the voltage output of a 10 kV power supply (Acopian model P010HD3). The RDMA was operated in stepping mode, which consisted of applying a fixed voltage and waiting 5 s at each voltage before the recording the average current over a 1 s measurement interval. While shorter waiting times (as short as 2 s) produced similar distributions, all measurements were done at 5 s waiting times to ensure steady state operation.

2.2.3. Instrument Coupling with Mass Spectrometer (in Collaboration)

The identity of the electrosprayed molecular ions was confirmed by affixing the nano-RDMA to the entrance of a mass spectrometer, as shown in figure 2.4. The components were assembled in series in the following order: electrospray source, nano-RDMA (second version), and Mass Spectrometer (Finnigan LCQ Deca Ion Trap Mass Spectrometer (LCQ-MS)). The electrospray source was the same used for calibration measurements and is more completely described in appendix I. The molecular ions measured in this arrangement were TPropylAI, TButylAI, TPentylAI, THexylAB, THeptylAB, and tetra octyl ammonium bromide (TOctylAB).

The electrospray source was connected to the nano-RDMA using standard Swagelok fittings. The nano-RDMA was positioned in front of the LCQ-MS using a breadboard plate (150 mm x 150 mm) made for mounting optical elements, a pair of custom-built plates, and optic mounting posts (O. D. ≈ 12 mm). The assembly aligned the sample outlet of the nano-RDMA with the atmospheric pressure inlet (API) of the LCQ-MS. Due to the ports on the nano-RDMA and the construction of the LCQ-MS, the sample outlet of the nano-RDMA and the API of the LCQ-MS were separated by a distance of 25 mm. The gap was reduced to less than 1 mm by attaching a Swagelok (1/4") to tube stub (1/8") fitting on the nano-RDMA outlet.

The nano-RDMA is operated with a 10 L min^{-1} sheath flow rate of nitrogen and in voltage stepping mode. The voltage on the DMA is provided from a high voltage power supply (Ultravolt 2 kV supply) that is controlled externally with a Labview program. The program set the voltage and then kept it constant for a 30-second interval, repeating this process for a fixed interval of voltages. The Labview program was started at the same time that a time-based scan in the MS software was started that had a duration long enough to ensure data would be collected over the complete voltage scan. The data were analyzed using a MatLab program that averaged the signal produced by the molecular ions over the 30-second interval that the voltage was held constant.

2.2.4. Instrument Comparison to Other DMAs (in Collaboration)

The performance in terms of transmission and resolution of the nano-RDMA was compared to the nano-DMA (cylindrical DMA designed for measuring nanoparticles in the 1–30 nm range) and the original RDMA (radial DMA designed for measuring nanoparticles in the 10–100 nm range). Four different monomers were measured in this study: tetra methyl ammonium iodide (TMAI), TPropylAI, THeptylAB, and tetra dodecyl ammonium iodide (TDodecAI).

The setup consisted of an electrospray source followed by a tandem DMA arrangement with two commercially available electrometers used as the detectors, as shown in figure 2.5. The electrospray source was similar to that described previously with the exception that the capillary was fused silica and the high voltage bias was provided through the solution. The first instrument was a high-resolution DMA (HR-DMA)[*9*] operating with a high sheath flow rate whose voltage was fixed at the peak of the monomer mobility distribution. The sampled outlet flow from the first DMA was split into two with one stream directed toward an electrometer for upstream concentration measurements and the other stream directed to the inlet of the second 'test' DMA.

The second DMA was operated in voltage stepping mode using recirculating sheath flow rates of 6 (data not shown), 10, and 15 L min^{-1} (data not shown). The aerosol flow rate was 0.6, 1, and 1.5 L min^{-1}, respectively. These flow rates were selected to maintain the aerosol to sheath flow rate ratio of 1:10, as is typical for aerosol measurements. The highest sheath flow rate tested was limited to 15 L min^{-1} as higher flow rates resulted in turbulence in the nano-RDMA. After collecting the mobility distributions for each ion, the signal from the second electrometer was normalized by that of the first electrometer to determine the particle transmission. The resolution was determined in the same way as in the calibration section.

2.3. Results

2.3.1. Calibration

From equation (2.1), the product Z_p*V is observed to depend on the DMA geometry and sheath flow rate. Based on this equation, the theoretical v_m*b was calculated to be 109.8 $\mathrm{cm}^2\ \mathrm{s}^{-1}$. Fitting the concentration distributions of the monomers and dimers for the previously reported salts, the experimental value was found to be $125.61 \pm 0.93\ \mathrm{cm}^2\ \mathrm{s}^{-1}$. Using this value, each voltage is converted to an inverse mobility ($1/Z_p$) and the distribution for each tetra-alkyl ammonium salt ion is shown in figure 2.6. The mobility distributions for the monomer and dimer are fitted well with two separate Gaussian distributions. As shown in figure 2.7, the measured mean inverse mobilities match the previously reported values over the entire range.

The experimental value for Z_p*V is 14.4% higher than theoretical estimate based on equation (2.1). The difference is partially due to non-uniformities in the electric field that were not taken into account in the derivation of equation. (2.1) , which therefore requires a higher voltage to classify ions of a known Z_p. The deviation occurs as the ions migrate toward the axis of the device. Here, the holes in the electrodes for the excess and sample flow outlet ports decrease the effective field ($E = V/b$). Although the excess flow outlet port is covered with a SS mesh, the field is nonetheless decreased. Also, the model assumes a radial source for the aerosol. In the actual device, the aerosol enters the classification region through a finite gap in the upper electrode between the knife edge (a) and the inner electrode (b), thus introducing uncertainty in the estimation of the radial distance. This is particularly problematic for the nano-RDMA since the gap is comparable in size to the radial distance to the knife edge. Hence, the mobility of the particles transmitted through the nano-RDMA is estimated using an empirical calibration factor, i.e.,

$$Z^* = \frac{Q_{sh} + Q_e}{2\pi(R_i^2 - R_e^2)} \frac{b}{V} \frac{1}{f_{mob}}, \tag{2.3}$$

where $f_{mob} = 0.874 \pm 0.009$.

As with the previous salt solutions, DMA scans of electrosprayed solutions of TEthylAI, TPentylAB and THexylAB revealed new peaks in the mobility spectra with reasonable inverse mobility values, plotted in figure 2.8. The measured inverse mobility distributions of these compounds are presented in figure 2.7. As before, each individual peak was fit with a Gaussian distribution. The mean inverse mobility found for each ion is listed in table 2.1 along with the values for the calibration standards.

2.3.2. Results: Mass Spectrometry

The mobility distribution recorded with the LCQ-MS for the monomer of each molecular ion is presented in figure 2.9. The molecular ion was detected at approximately the same voltage reported previously when a Faraday cup electrometer was used as the detection, confirming the identity of the molecule detected. The spectra are plotted with error bars corresponding to the standard error of the signal, demonstrating that a 30-second interval produces a stable signal.

An extended voltage scan was captured to confirm the identity of the dimer and trimer peak for THeptylAB, as shown in figure 2.10. The mass spectrum for the monomer peak consisted of a single mass at a molecular weight of 410. The region corresponding to the dimer region consisted of three different species: monomer, dimer, and doubly charged quadramer. The monomer is most likely due to transmission through the nano-RDMA of the dimer followed by fragmentation upon reaching the API of the LCQ-MS, but this has not been proved. Detection of the doubly charged quadramer is not unexpected as it should have the same mobility as the singly charged dimer. The third peak in the distribution consisted of more molecular weights than the first, including the monomer, dimer, trimer, and quadramer, indicating that this peak is not due to a monomobile species.

2.3.3. Results: DMA Comparison

A plot of the normalized mobility spectra for the molecular ions analyzed with the nano-RDMA and the nano-DMA as the "test" DMA are presented in figure 2.11. The mobility spectra for the salts with the three largest monomers were narrow, single modal distributions. Comparing the nano-RDMA and the nano-DMA data, the transmission was observed to be approximately a factor of three and five higher (not shown) for the nano-RDMA compared to the nano-DMA and RDMA, respectively. Interestingly, the mobility spectra for the TMAI monomer contained three separate peaks, as shown in figure 2.12. Three separate peaks were not observed in the mobility spectra using the other DMAs. It was determined that the second and third peak were due to methanol (or an impurity in the methanol solvent) clusters that transmitted the HR-DMA[*9*] in a multiply charged state and discharged one and two electrons, producing less mobile species. The presence of three peaks in the mobility spectra for the TMAI molecular ion made the data unsuitable for transmission analysis.

2.4. Discussion

2.4.1. Calibration

An important figure of merit for size measurements is the instrument mobility resolution, which is defined as the ratio of the mean particle mobility over the full width at half maximum of the mobility distribution:[*5*]

$$\Re = \frac{Z_P}{\Delta Z_{P,FWHM}} . \tag{2.4}$$

In the non-diffusive limit, the theoretical resolution equals $\Re_{nondiff} = Q_{sh}/Q_a$, which corresponds to a value of 16.7 ($Q_{sh}/Q_a = 10/0.6$) for the conditions used in this experiment. When the ratio eV/kT is small, Brownian diffusion degrades the resolution, which becomes proportional to $V^{1/2}$. Flagan[5] showed that the resolving power of an ideal DMA operated in the diffusive limit is

$$\Re_{diff} = 0.425\left[\frac{Pe_{mig}}{G_{mig}}\right]^{\frac{1}{2}} , \tag{2.5}$$

where, for the RDMA, $Pe_{mig} = eVf_{mob}/kT$. The factor, G_{mig}, depends upon the sheath and aerosol flow rate as well as the particulars of the DMA geometry and the assumed gas flow profile. The non-diffusive and diffusive resolution limits can be combined to compare with the measured resolutions,[*7*] according to the following equation:

$$\Re_{Exp} = \sqrt{\left(\frac{1}{R^2_{nondiff}} + \frac{1}{R^2_{diff}}\right)^{-1}} . \tag{2.6}$$

Measurements made using monomobility ions enables direct determination of the mobility resolution from the widths of the mobility peaks seen in figures 2.6 and 2.8. Experimentally, the instrument resolution was calculated for each molecular ion monomer and dimer from the mobility distribution fits found previously and plotted in figure 2.13. Over the range of voltages used, the resolution of the monomeric molecular ion (M^+) is found to increase with voltage with approximately the same slope as that predicted in the diffusive (high mobility/small particle) limit. The observed resolution is clearly smaller than predicted when assuming uniform parallel flow and uniform electrical fields. Empirically for the nano-RDMA, we find $G_{mig} = 17.3 \pm 1.1$; this deviates from the simplistic model estimate of $G_{mig} = 10.5$. One possible explanation for the observed resolution being lower than theoretically predicted is the possibility of a recirculation bubble near the stagnation point on the axis of the instrument.[*16*] Regardless of the cause of deviation, the nano-RDMA is observed to operate in the diffusive limit for the range of mobilities of the molecular ions measured in this study. Yet, the instrument clearly demonstrates resolving ability for particle mobilities that were not even measurable with the original RDMA.

For the dimer molecular ions ($(MX)M^+$), the measured resolution falls below that of the monomer ions, but they appear to follow the same $V^{1/2}$ power law. The data preclude the possibility that the resolution begins to degrade as the voltage increases since the THeptylAB monomer resolution follows the $V^{1/2}$ trend of the monomers and is measured at nearly the same voltage as the TPropylAI dimer. While not rigorously tested, the observed difference in the trends of the resolution for the monomers and the dimers could be due to the non-spherical nature of the dimer. As observed for significantly larger particles[*17*] classified at low voltages (i.e., <2000 V), the dimers tend to migrate through the DMA with an orientation that approaches random. Since the orientation of the dimer can affect the drag force, the dimers will be transmitted over a broader range of voltages leading to a lower effective mobility.

The results presented above have been discussed in terms of inverse mobility, but this quantity is hard to visualize. The real-space analog of inverse mobility is diameter. In the free-molecular limit, the mobility diameter is larger than the physical particle diameter by 0.3 to 0.4 nm.[*18*] The observed difference between the two diameters corresponds to the radius of the background gas molecules. In terms of mobility diameter, particle sizes as small as 1.03 nm (TEthylAI monomer ion) were sized with a standard geometric deviation (σ_g) of 1.05 (Resolution of ~4.7). Resolution increased with diameter reaching a value of ~7 at 1.47 nm (monomer ion of THeptylAB), which corresponds to a σ_g of 1.035. In other words, this instrument can differentiate a particle with a diameter of 1.0 nm from a particle with a diameter 1.1 nm. More importantly, this instrument has the necessary resolving power to distinguish growth by vapor deposition from that by coagulation down to a mobility diameter of 1 nm, since the experimentally observed σ_g is much smaller than the self-preserving distribution value of about 1.3 associated with coagulation. Beyond measuring the size of molecular ions, the instrument can be utilized for larger ions. Based upon the empirical calibration constant determined from measuring molecular ions, the upper size limit for the sheath flow rate investigated here is calculated to be 13 nm. To characterize the instrument response for particles larger than 1.8 nm will require additional measurements using the tandem DMA technique or larger molecular ions.

2.4.2. Mass Spectrometry

The mass spectrometer confirmed the molecular weight of the electrosprayed monomers unambiguously. The instrument resolution could be calculated from the mobility spectra to be a value of 7 for the THeptylAB monomer. This is similar but slightly lower than what was observed when detecting the ions with a faraday cup electrometer. The exact origin of the difference was not determined, but it could be related to the introduction of the ions through the API. The resolution could be readily changed through adjusting the aerosol flow, as expected. This adjustment could be valuable in cases where slightly higher resolution is needed. Yet, the flow rate adjustment has an impact on the transmission to the LCQ-MS, and the standard error of the distribution increases.

The mass measurements provided significant information about the dimer peak. A significant fraction of the total signal from the dimer peak is observed at the molecular weight of the monomer. Detection of the monomer is most likely a by-product of dimer fragmentation upon entering the API of the LCQ-MS. In addition to the monomer and dimer, the doubly charged quadramer was detected in the second peak. The presence of the quadramer could be partially responsible for the lower resolution of the dimer peak reported for the instrument calibration.

The mass analysis of the third peak in the mobility spectrum confirmed previous expectations that the third peak in the mobility distribution was not due to a single species. This peak is most likely a multiply charged species containing several of the molecular ions that evaporates upon entering the API of the LCQ-MS and therefore is not appropriate for determining the resolution.

2.4.3. DMA Comparison

The tandem DMA experiments provided important information about the transmission and resolution of the nano-RDMA in comparison to other similar devices. The transmission increased with molecular ion size since fewer particles are lost to diffusion as the particle size increase. The measured transmission was higher than the other devices tested, but could be improved with a better design of the aerosol inlet extension (simulations discussed in chapter 3). Still, the higher transmission of the nano-RDMA offers the ability to detect lower particle concentrations that could be invaluable in field measurements. Also, having the transmission information permits a more accurate description of the concentration of unknown aerosol sources.

The resolution of the nano-RDMA was also higher than the other DMAs tested. The detection of multiple peaks in the TMAI mobility spectra addresses the importance of resolution in mobility measurements. The first DMA transmitted multiple species of different charge states. Without the higher resolution offered with the nano-RDMA (higher than the other DMAs compared), the transmission data would be improperly calculated. The multiply charged particles would produce a greater current in the first electrometer than singly charged particles would produce in the second electrometer.

2.5. Summary

We described a nano-RDMA that enables the classification of molecular ions with mobility diameters in the range of 1 to 1.8 nm. The instrument was calibrated using monomer ions. Non-uniformities in flow and electric field emanating from the very short classification region required empirical corrections to the predicted mobility response and resolution from which an upper limit for size measurement was calculated to be 13 nm.

While the nano-RDMA operates in the diffusive limit for these molecular ions, its resolving power is, nonetheless, substantial and should enable investigation of aerosol or nanoparticle growth dynamics at mobility diameters as small as 1 nm.

Coupling of the nano-RDMA with the LCQ-MS confirmed the identity of the molecular ions as well as provided information about the other peaks. The resolution of the monomer peak was slightly lower than that measured for the calibration. The dimer peak was found to contain a significant fraction of monomer and dimer molecular weights as well as a small amount of doubly charged quadramers. The heterogeneity of this peak could contribute to the lower-than-expected resolution for the dimer peak.

Comparing the nano-RDMA operation with similar DMAs showed that the transmission and resolution were higher for this device. The higher resolution proved valuable as the nano-RDMA was able to detect multiple peaks in the mobility spectra of TMAI. The high transmission and resolution demonstrated in these measurements will make the nano-RDMA an attractive option when selecting a mobility measuring device.

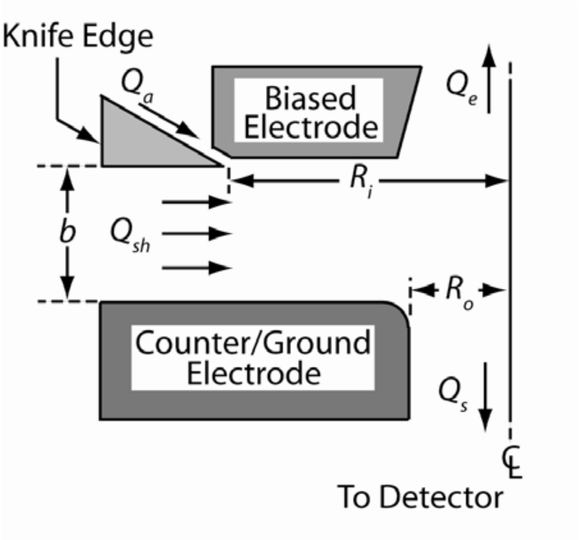

Figure 2.1. Simplified Schematic of RDMA Operation.

Simplified schematic of the nano-RDMA operation illustrating the direction of the sheath gas flow (Q_{sh}), the aerosol inlet (Q_a), the sampled outlet (Q_s), and the excess flow outlet (Q_e).

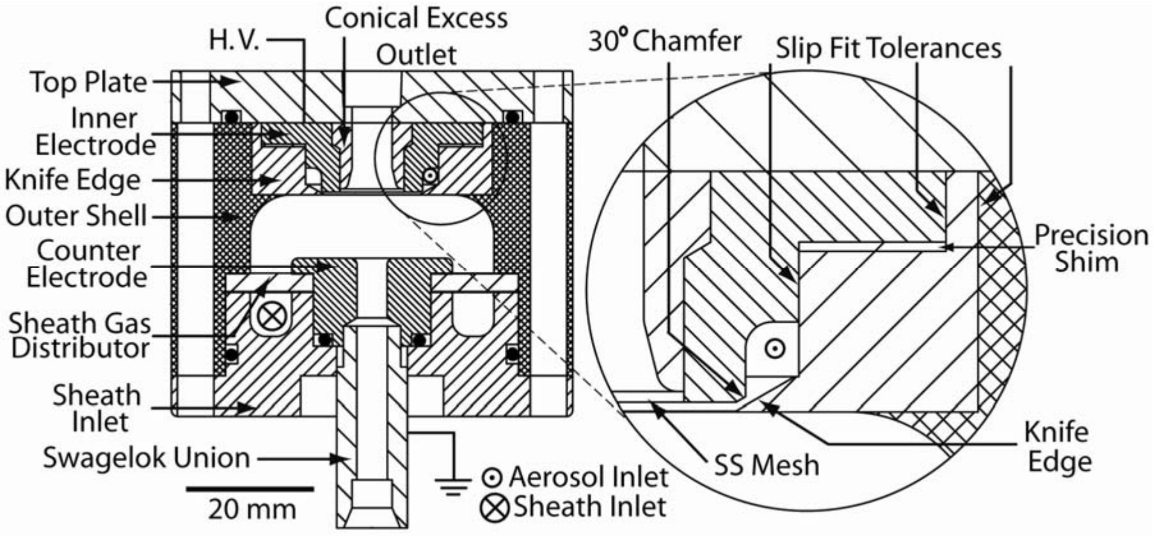

Figure 2.2. Detailed Schematic of the nano-RDMA.

Detailed schematic of the nano-RDMA. The materials used for construction are noted in the text. Filled circles represent O-Rings. The inset depicts the slip-fit tolerances and the knife edge in more detail as well as the location where precision shim disks are placed to create a gap between the chamfer and the knife edge through which the aerosol leaves the racetrack and enters the sizing portion of the device.

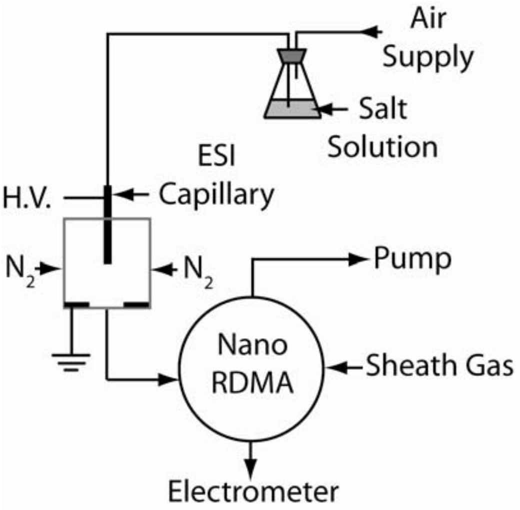

Figure 2.3. Schematic of Electrospray.

Schematic of electrospray and nano-RDMA combination used to measure molecular ions and determine the resolution of the nano-RDMA.

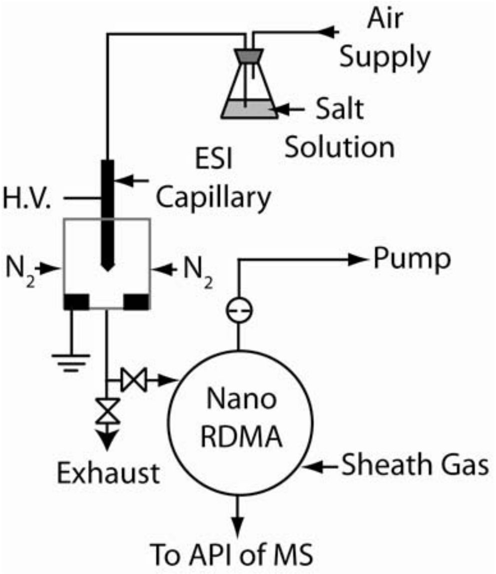

Figure 2.4. Schematic of nano-RDMA and Mass Spectrometer.

Schematic of the experimental set up used to measure the combined mobility and mass distribution.

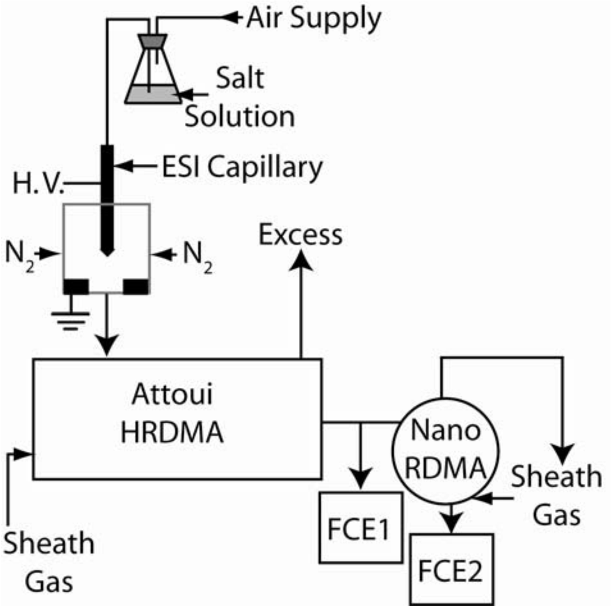

Figure 2.5. Schematic of TDMA.

Schematic of the tandem DMA arrangement used to determine transmission and resolution of the second DMA.

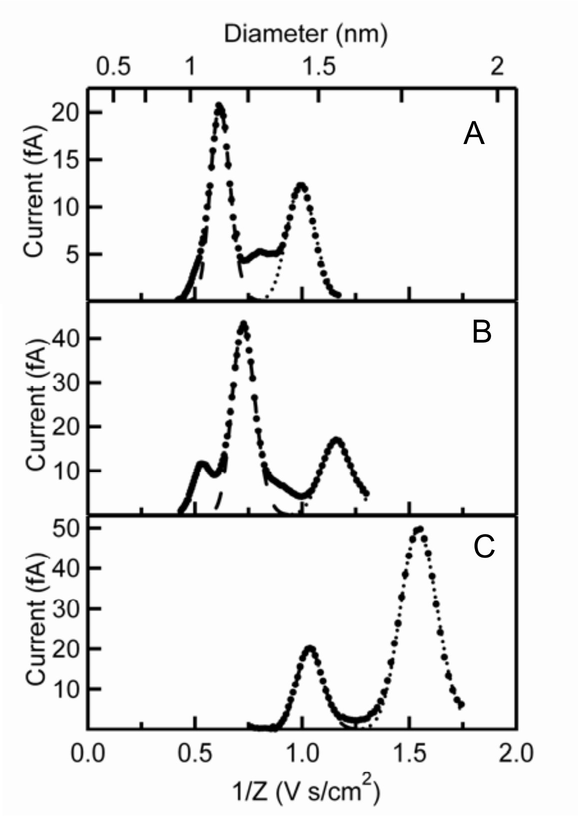

Figure 2.6. Inverse Mobility Distributions.

Inverse mobility distributions of (A) TPropylAI, (B) TButylAI, and (C) THeptylAB. The long dash curve fits the M^+ (i.e., R_4N^+) distribution and the short dash curve fits the M_2X^+ distribution. The mobility values plotted are scaled values.

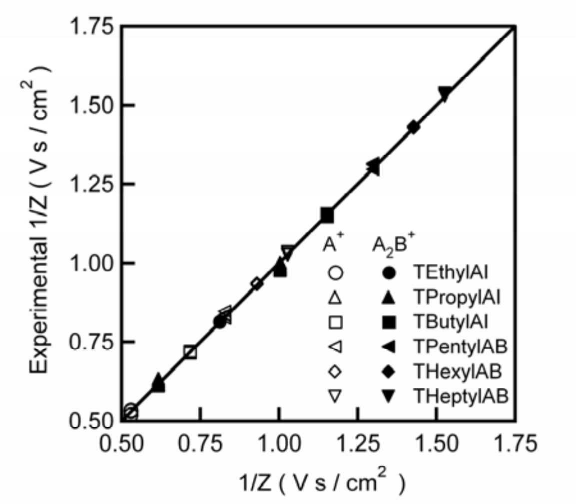

Figure 2.7. Geometric Mean Mobilities.

Compilation of the geometric mean mobilities obtained from fitting size distributions plotted versus the mobility found previously (Ude and de la Mora 2005). The empty symbols are for the monomer and the filled symbols are for the dimer.

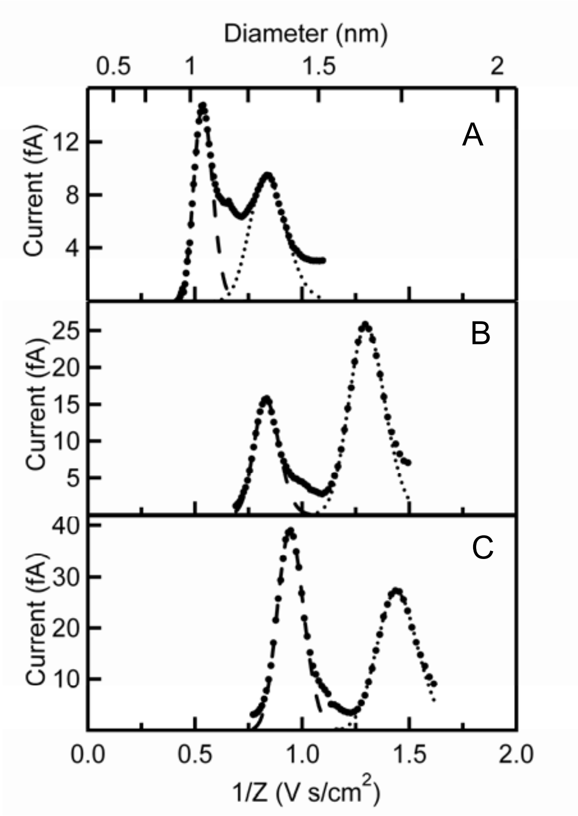

Figure 2.8. Inverse Mobility Distributions.

Inverse mobility distributions of (A) TEthylAI , (B) TPentylAB, and (C) THexylAB. The long dash curve fits the M^+ (i.e., R_4N^+) distribution and the short dash curve fits the M_2X^+ distribution. The mobility values plotted are scaled values.

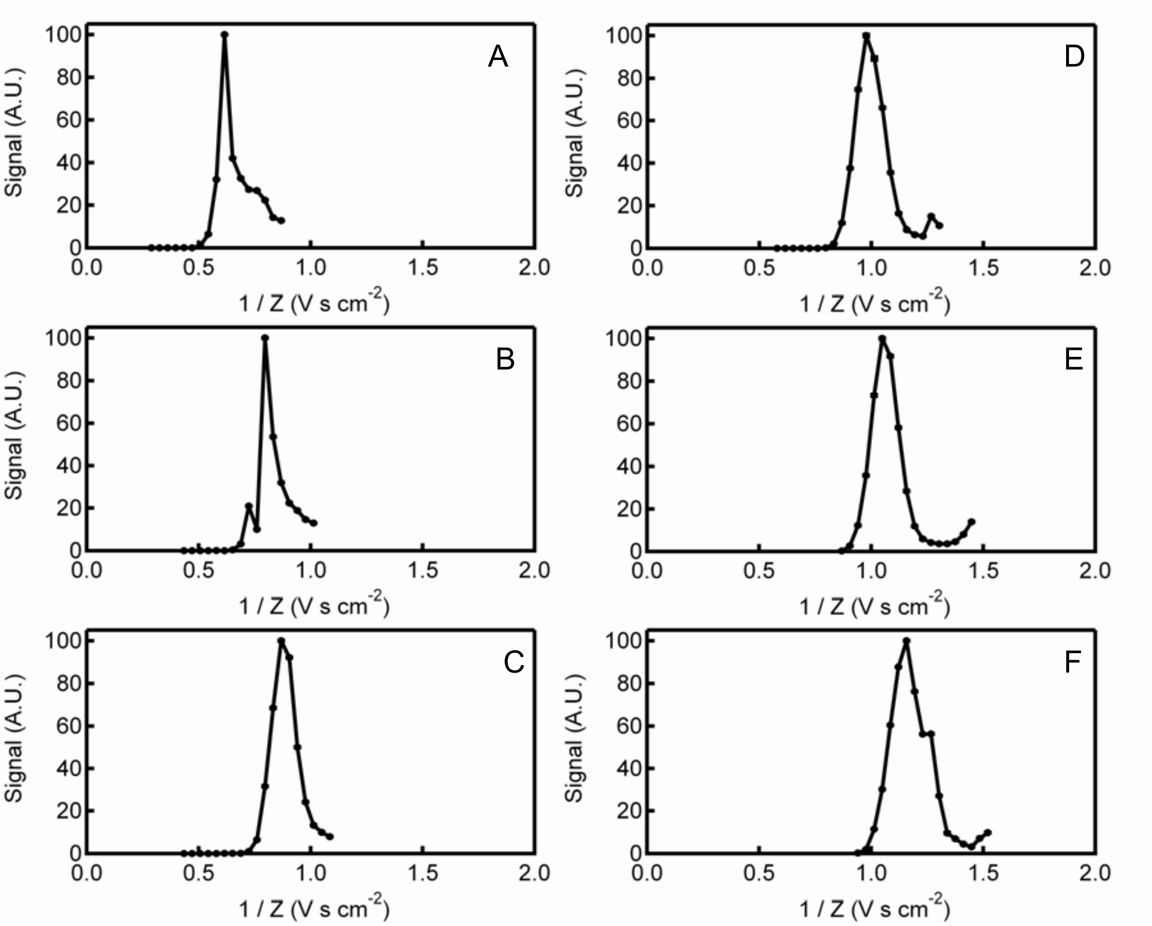

Figure 2.9. Inverse Mobility Distributions Using Mass Spectrometer as Detector. Inverse mobility spectra recorded with the LCQ-MS for the monomer of (A) TPropylAI, (B) TButylAI, (C) TPentylAI, (D) THexylAB, (E) THeptylAB, and (F) TOctylAB.[*]

---

[*] The mobility spectra were recorded with a sheath flow rate of 11 L min^{-1}. The data have been corrected to account for the higher flow rate.

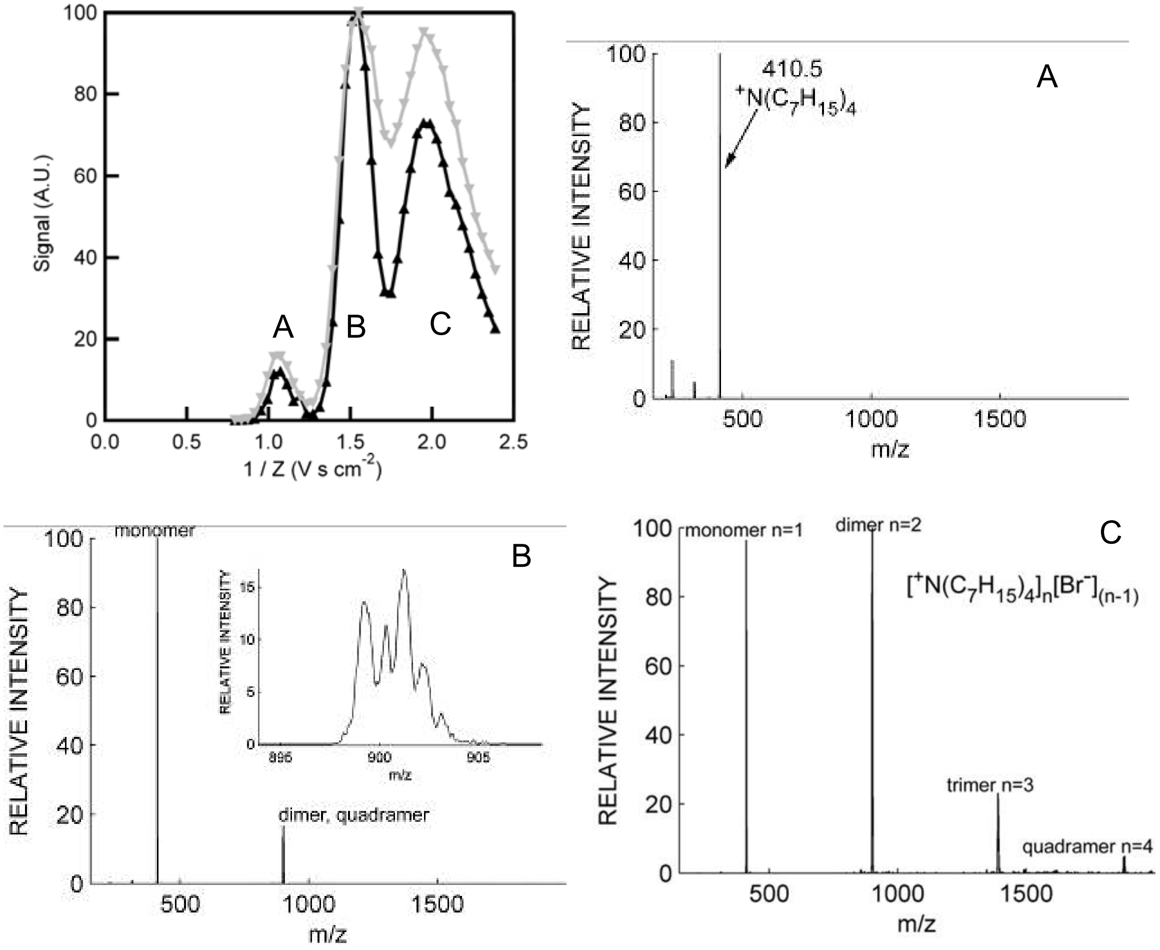

Figure 2.10. Mobility Distribution of Monomer and Dimer Using MS.

Extended mobility spectra capturing the monomer (A), the dimer (B), and a third peak (C) for the high resolution (black triangles up; Q_a = 500 sccm) and low resolution (gray triangles down; Q_a = 1000 sccm) cases. (A) The mass spectra for the monomer region of the mobility distribution. (B) The mass spectra for the dimer region of the mobility distribution with the inset depicting the presence of the doubly charged quadramer. (C) The mass spectra for the third peak of the mobility distribution indicating the presence of trimer and quadramer.

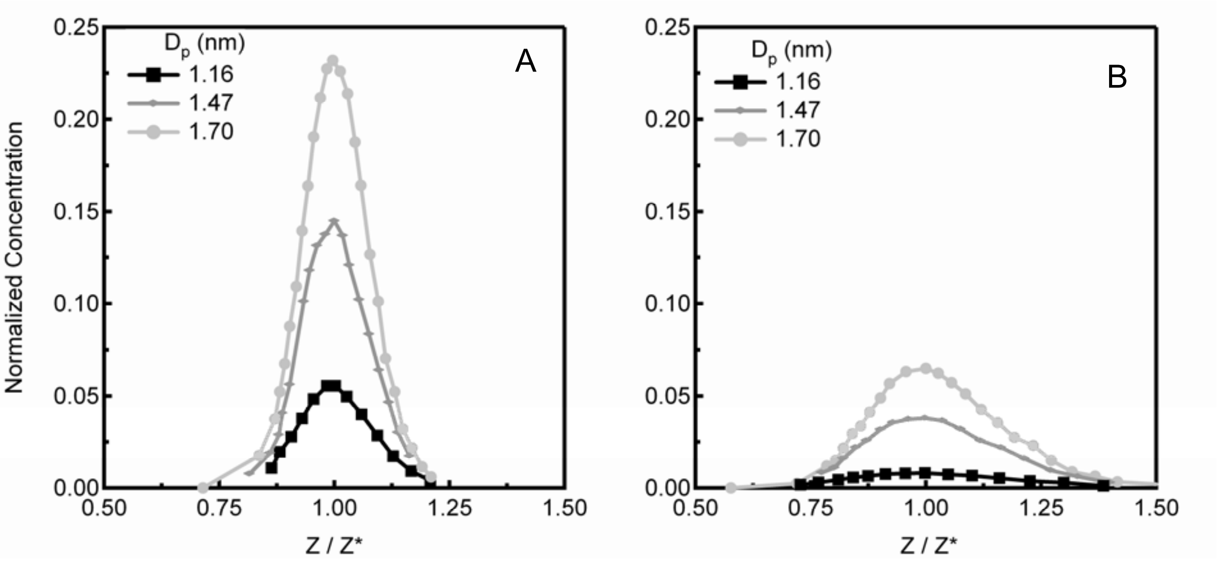

Figure 2.11. Mobility Distribution Comparison between nano-RDMA and nano-DMA.

(A) Normalized mobility spectra for molecular ions of different size measured with the nano-RDMA. (B) Normalized mobility spectra for molecular ions of different size measured with the commercial nano-DMA. The calibration standards are the molecular ions used previously: D_p of 1.16 nm is TPropylAI, 1.47 is THeptylAB, and 1.70 is TDodecylAI.

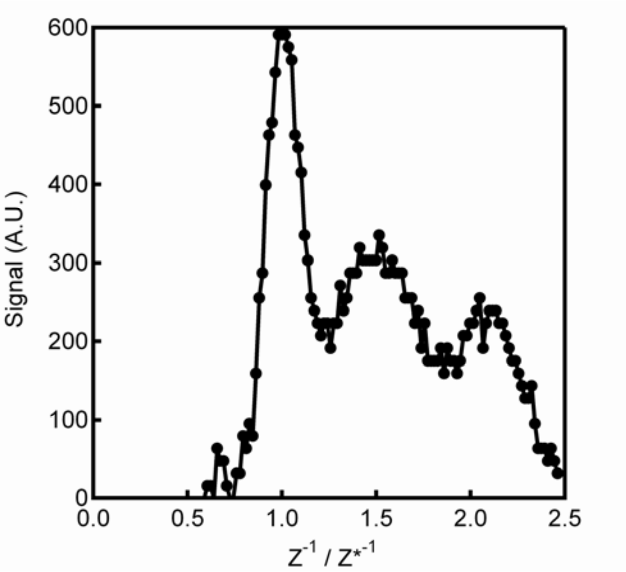

Figure 2.12. Mobility Distribution of TMAI.

Mobility spectra recorded with the nano-RDMA of a stream containing TMAI that is size selected with a HR-DMA. The first peak is due to the molecular ion TMAI whereas the second and third peaks have been determined to be due to either methanol clusters or impurities in the methanol.

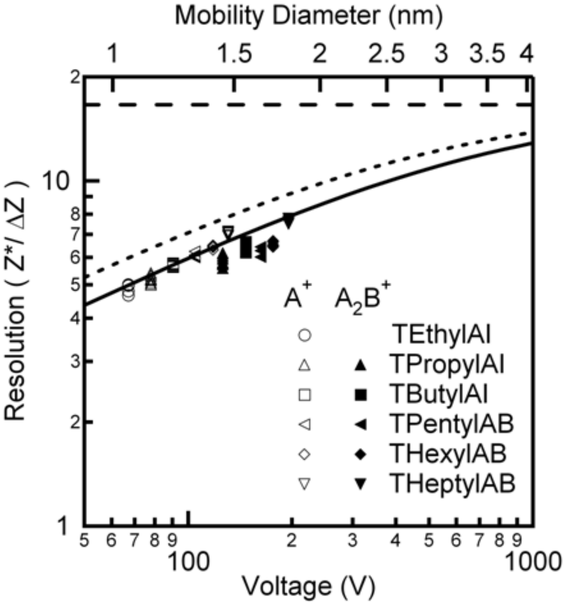

Figure 2.13. nano-RDMA Resolution.

Comparison of the theoretically calculated and experimentally measured resolution. The empty symbols correspond to the monomer whereas the filled symbols are for the dimer. The solid line corresponds to the fit of the experimental data while the dashed lines are the calculated theoretical limits in the diffusion regime (short dash) and in the absence of the effects of diffusion.

Table 2.1. Mobility Data.

Previously determined and experimentally measured inverse mobilities for each of the different tetra-alkyl ammonium salts as well as the calculated resolution. The values listed under the heading M^+ corresponds to monomers for the appropriate molecular ion whereas the values listed under $(MX)M^+$ correspond to the dimers.

Molecular Ion	Previous $1/Z^*$ (cm^2/V s)	Mean V (V)	Mean $1/Z$ (cm^2/V s)	Standard Deviation (cm^2/V s)	Mean Resolution	Standard Deviation
M^+						
TEthylAI	-	66.6	0.531	0.007	4.88	0.15
TPropylAI	0.619	77.8	0.619	0.007	5.18	0.14
TButylAI	0.718	90.5	0.721	0.002	5.70	0.06
TPentylAB	-	105.1	0.837	0.006	6.07	0.09
THexylAB	-	117.7	0.937	0.001	6.42	0.06
THeptylAB	1.030	129.6	1.032	0.004	7.02	0.08
$(MX)M^+$						
TEthylAI	-	102.7	0.8177	0.007	-	-
TPropylAI	1.006	124.5	0.991	0.009	5.89	0.22
TButylAI	1.153	145.3	1.157	0.003	6.39	0.22
TPentylAB	-	164.8	1.312	0.010	6.23	0.21
THexylAB	-	180.0	1.433	0.002	6.51	0.11
THeptylAB	1.529	193.1	1.537	0.004	7.62	0.10

---

[*] Ude and de la Mora, 2005.

References

1. E. Knutson, and K. Whitby, *Journal of Aerosol Science,* **6**, 443, 1975.
2. R. Flagan, *Aerosol Science and Technology,* **28**, 301, 1998.
3. P. McMurry, *Atmospheric Environment,* **34**, 1959, 2000.
4. M. Stolzenburg, University of Minnesota (1988).
5. R. Flagan, *Aerosol Science and Technology,* **30**, 556, 1999.
6. D. Chen, D. Pui, D. Hummes, H. Fissan, F. Quant, and G. Sem, *Journal of Aerosol Science,* **29**, 497, 1998.
7. J. Rosell-Llompart, I. Loscertales, D. Bingham, and J. Fernandez de la Mora, *Journal of Aerosol Science,* **27**, 695, 1996.
8. L. De Juan, and J. Fernandez de la Mora, *Journal of Aerosol Science,* **29**, 617, 1998.
9. S. Rosser, and J. Fernandez de la Mora, *Aerosol Science and Technology,* **39**, 1191, 2005.
10. P. Martínez-Lozano, and J. de la Mora, *Journal of Aerosol Science,* **37**, 500, 2006.
11. S. Zhang, Y. Akutsu, L. Russell, R. Flagan, and J. Seinfeld, *Aerosol Science and Technology,* **23**, 357, 1995.
12. H. Fissan, A. Pöcher, S. Neumann, D. Boulaud, and M. Pourprix, *Journal of Aerosol Science,* **29**, 289, 1998.
13. R. Sankaran, D. Holunga, R. Flagan, and K. Giapis, *Nano Letters,* **5**, 537, 2005.
14. Y. Kousaka, K. Okuyama, M. Adachi, and T. Mimura, *Journal of Chemical Engineering of Japan,* **19**, 401, 1986.
15. S. Ude, and J. Fernandez de la Mora, *Journal of Aerosol Science,* **36**, 1224, 2005.

16. J. Fernandez de la Mora, *Journal of Aerosol Science,* **33**, 411, 2002.

17. A. Zelenyuk, Y. Cai, and D. Imre, *Aerosol Science and Technology,* **40**, 197, 2006.

18. H. Tammet, *Journal of Aerosol Science,* **26**, 459, 1995.